Metal–Ligand Redox in Layered Oxide Cathodes for Li-ion Batteries

Matthew J. W. Ogley,[1,2,§] Ashok S. Menon,[1,2,§], Gaurav Pandey,[1] Galo J. Páez Fajardo,[1,2] Beth J. Johnston,[2,3] Innes McClelland,[2,3] Veronika Majherova,[1,2] Steven Huband,[4] Debashis Tripathy,[2,5] Israel Temprano,[2,5,6] Stefano Agrestini,[7] Veronica Celorrio,[7] Gabriel E. Pérez,[8] Samuel G. Booth,[2,3] Clare P. Grey, [2,5] Serena A. Cussen,[2,3] and Louis F. J. Piper[1,2*]

[1] *Warwick Manufacturing Group, University of Warwick, Coventry, CV4 7AL, UK*
[2] *The Faraday Institution, Quad One, Harwell Campus, Didcot OX11 0RA, UK*
[3] *Department of Materials Science and Engineering, The University of Sheffield, Sheffield, S1 3JD, UK*
[4] *Department of Physics, University of Warwick, Coventry, CV4 7AL, United Kingdom*
[5] *Department of Chemistry, University of Cambridge, CB2 1EW, UK*
[6] *CICA-Centro Interdisciplinar de Química e Bioloxía and Departamento de Química, Facultade de Ciencias, Universidade da Coruña, 15071, A Coruña, Spain*
[7] *Diamond Light Source Ltd., Harwell Science and Innovation Campus, Didcot, OX11 0DE, UK*
[8] *ISIS Neutron and Muon Source, Rutherford Appleton Laboratory, Harwell Science and Innovation Campus, Didcot, OX11 0QX, UK*

§ These authors contributed equally to this work.
* Corresponding author email addresses: Louis.Piper@warwick.ac.uk

Key Words: O-Redox, Ligand Holes, Charge Compensation, Ni-rich cathodes, NMC811, XAS, RIXS, SAXS

Abstract

Understanding charge compensation in Li-ion battery cathodes is crucial for improving specific capacity and cycle life. This study clarifies some of the ambiguities and inaccuracies of the commonly used ionic-bonding model that requires separate transition metal (TM) and oxygen redox regimes, using an archetypal layered oxide cathode, $LiNi_{0.8}Mn_{0.1}Co_{0.1}O_2$. Contrary to the prevalent TM-centric ionic model, this research reveals that charge compensation upon Li removal occurs without formal Ni oxidation. Instead, oxygen dominates the redox process, facilitated by strong TM–O hybridisation, forming bulk stable $3d^8\underline{L}$ and $3d^8\underline{L}^2$ electronic states, where $\underline{L}$ is a ligand hole. This model supports the observation of O K-edge resonant inelastic X-ray scattering features, often attributed to bulk O–O dimers, irrespective of the state of delithiation. Furthermore, there is no evidence of any crystallographic TM migration or void formation. Above 4.34 V vs. Li^+/Li, the cathode loses surface O, forming a resistive surface rock salt layer that eventually causes capacity fade. This highlights the importance of cathode engineering when attempting to achieve higher energy densities with layered oxide cathodes where O dominates the charge compensation process.

1. Introduction

The specific capacity (mAh g⁻¹) of layered oxide cathodes in Li-ion batteries is primarily limited by the operational voltage window over which they can be cycled. Efforts to increase the specific capacity, and by extension, the energy density (Wh g⁻¹/ Wh L⁻¹), are therefore focused on widening this voltage window without compromising long-term cycling stability. However, this is not a straightforward task as increasing the upper cut-off voltage exacerbates cathode degradation.[1,2] The routes by which this degradation occurs are closely linked with an electronic charge compensation mechanism that results in a more oxidised cathode at high states of delithiation. This primes the cathode for reactivity with the electrolyte.[2] Therefore, an accurate description of the charge compensation process is necessary to decouple voltage limits from degradation and inform strategies that aim to improve long-term electrochemical performance.

In conventional layered oxide cathodes of the form LiTMO$_2$ (where TM is a 3d transition metal), delithiation is facilitated by an electronic charge compensation mechanism that is conventionally described using a simple ionic-bonding model.[3] Here, TM cations and O anions are considered to possess discrete redox-active electronic bands, as depicted in Figure 1a. Due to the alleged stability of the closed-shell 2p^6 configuration of O^{2-}, the redox-active states located at the Fermi energy are assumed to originate solely from the TM 3d orbitals; hence the term 'TM redox'. However, for mid-to-late TM-containing systems such as LiNi$_{0.8}$Mn$_{0.1}$Co$_{0.1}$O$_2$, the effects of oxidised O are strongly pronounced.[4] This is often overlooked when describing charge compensation in these systems. Therefore, even though the ionic-bonding model does acknowledge the role of the ligand via crystal field splitting, in practice, this approximation is inaccurate and needs to be developed further.

The ionic model may be improved by utilising band theory with a Hubbard U correction allows for the consideration of electron correlations and charge-transfer (CT) energies, thus better representing the interactions occurring in a crystalline solid. This complex multi-electron physics can successfully assign the redox activity of negative CT insulators to the ligand due to the relative positions of the anionic O 2p band versus the filled lower Hubbard band (Figure 1b).[5,6] Corroborating this, ligand-dominated electronic ground states have been observed in both LiNiO$_2$ and LiCoO$_2$,[7-10] thereby disproving the applicability of the ionic bonding model to these systems. However, despite band theory better considering the energy of the ionic components and their respective electronic interactions, highly covalent systems that exhibit shared orbital character require additional explanation.[11-15] Ligand field theory (LFT) can be adapted into one such model. Like the simple ionic-bonding model, many molecular orbital (MO) descriptions using LFT do not always account for the relative distribution of TM and ligand orbital energy levels. This has significant effects for late TMs (e.g., Ni, Cu) where greater effective nuclear charge results in more 'core-like' 3d orbitals, which stabilises them below the ligand group orbitals. This causes the resultant ligand field to invert, with the antibonding highest occupied molecular orbital being dominated by ligand character (Figure 1c).[16,17] Such a unique interaction was first proposed for [Cu(CF$_3$)$_4$]⁻; initially considered to be a formal Cu(III) complex, it was instead confirmed to have a 3d^{10} electronic configuration, with the remaining charge balanced by oxidised perfluoromethyl ((CF$_3$)$_4$) ligands.[16,18,19] Similarly, many different formal Ni(IV) complexes also show comparable behaviour, with none surpassing a 3d^8 electron count, one which is conventionally assigned to Ni^{2+} by the ionic bonding

2

model.[20] Not only does this imply an inherent ligand-impartiality, but it also suggests that the degree of anionic charge compensation is more greatly determined by the coordination environment, d electron count and effective nuclear charge of the central *TM* cation.[17] Taken together, this makes the assignment of late-*TM* oxidation states more difficult than for early-*TMs*.[21] This complexity obfuscates the true definitions of TM and O redox and outlines the importance of proper definitions and suitable models when investigating charge compensation.
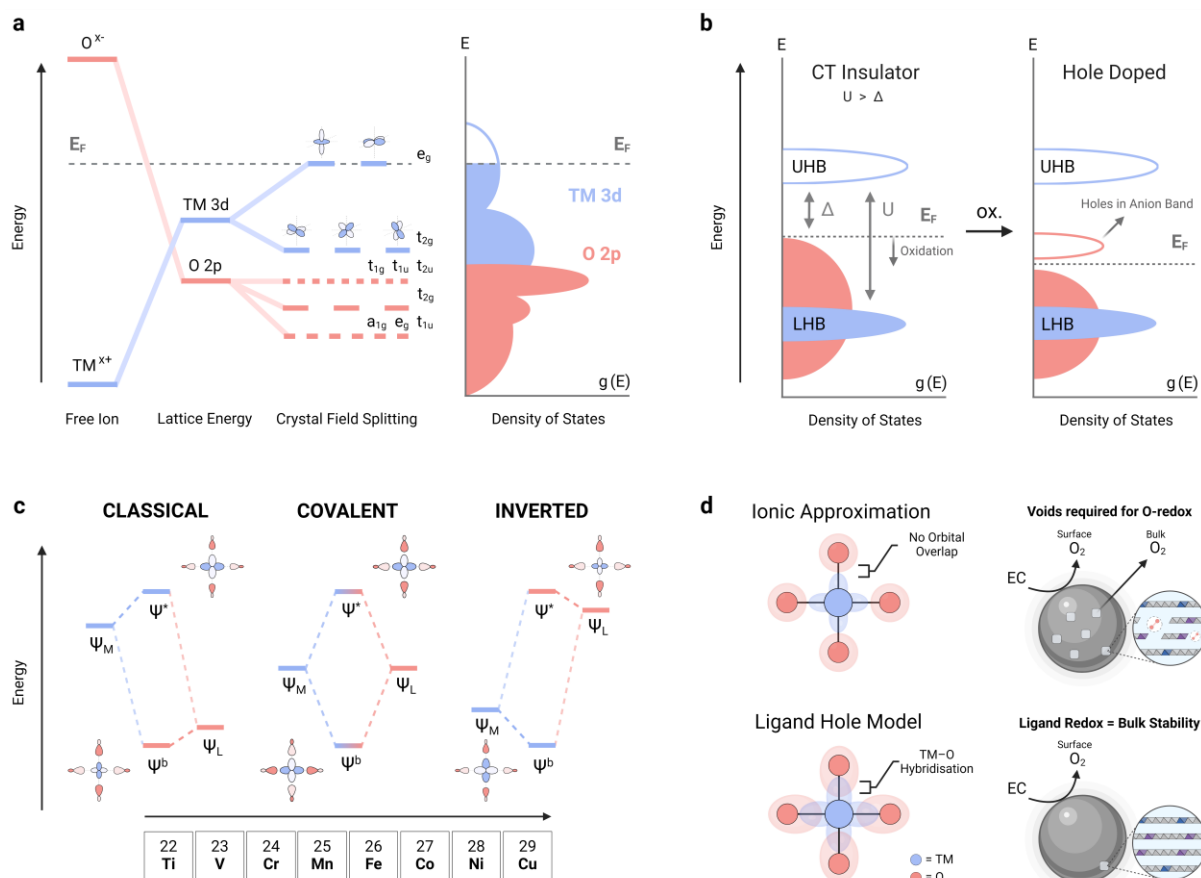
Figure 1: (a) Qualitative TM and O atomic orbital energies at different stages of the ionic-bonding model, along with a corresponding density of states. (b) Band structures of negative charge-transfer (NCT) and hole-doped NCT systems. UHB and LHB stands for upper and (filled) lower Hubbard bands, respectively. (c) MO diagrams for a TM–O_6 octahedron in classical, covalent, and inverted ligand fields. The effect of increasing the effective nuclear charge, Z_{eff}, is depicted below.[16] (d) Schematic illustration of the two electronic structure models proposed for Ni-rich layered oxide cathodes, and how they can explain the consequences of delithiation at the cathode bulk and surface.

In current nomenclature, *TM*-redox encompasses all electronic charge compensation involving *TM* d orbitals, regardless of the possible contributions of hybridised anionic ligands.[22] Conversely, discrete O-redox involves the depopulation of unhybridised O 2p orbitals, such as those formed along Li–O–Li moieties in Li-rich layered oxides.[23] The ionic charge compensation model is invoked to explain the 'anomalous' first-charge capacity of layered Li-rich oxide cathodes such as $Li_{1.2}Mn_{0.54}Ni_{0.13}Co_{0.13}O_2$ and describes two separate *TM* and O oxidation regimes [24,25]. Such a description is based on the spectral evolution of the *TM* K-edges ceasing in energy close to 4.5 V (vs. Li^+/Li), thereby allegedly marking the end of '*TM* oxidation' and the onset of 'O oxidation'.[26,27] Evidence of O oxidation was

3

obtained with high-resolution O K-edge resonant inelastic X-ray scattering (RIXS), wherein charging from 4.5 to 4.8 V resulted in the growth of new spectral features.[28] Owing to their similarity to gaseous molecular O_2, they were interpreted as neutral 1.2 Å O–O dimers that formed in the cathode bulk.[28] Nonetheless, it is worthwhile to reconsider the suitability of the ionic bonding model in explaining these observations. Firstly, the trace occurrence of the RIXS features at voltages as low as 4.5 V suggests that O–O dimers may have already begun to form prior to the alleged 'O oxidation' regime.[28] Therefore, if O dimerisation were solely a consequence of O oxidation, a separate mechanism that also results in oxidised O must occur during *TM* oxidation. Secondly, the same high-resolution RIXS features have also been observed in delithiated stoichiometric (Li:*TM* = 1) layered oxide cathodes,[29-31] systems which need not invoke discrete O-redox in explaining their practical capacity. Considering the differences in the stoichiometry, pristine structure, and delithiation pathway between Li-rich and stoichiometric layered oxide cathodes, consolidating the mechanism responsible for O–O dimerisation and its role in charge compensation remains challenging when using a simple ionic model. However, through applying and validating a ligand-centred redox model, the existence of oxidised O can be explained without requiring any bulk crystallographic differences like TM migration or voids (Figure 1d).

In this study, the electronic charge compensation mechanism during the electrochemical (de-)lithiation of a commercial layered oxide cathode material, $LiNi_{0.8}Mn_{0.1}Co_{0.1}O_2$, is revisited through multi-scalar X-ray spectroscopy. Using (*ex situ*) hard and soft X-ray absorption spectroscopy measurements, aided by online electrochemical mass spectroscopy and theoretical spectral simulations, the evolution of the TM and O electronic structures at the bulk, sub-surface (100–200 nm) and surface as a function of delithiation is characterised. Further investigation of the O electronic structure changes, specifically the possible dimerisation process, were carried out through high-resolution O K-edge RIXS spectroscopy. Corresponding measurements were also performed on other layered oxide cathodes, $LiCoO_2$ and $Li_{1.2}Mn_{0.54}Ni_{0.13}Co_{0.13}O_2$, to understand whether differences in the stoichiometry, pristine structure, and delithiation pathway, influenced the nature of O participation (i.e., dimerisation) in the charged states. Furthermore, the relevance of the findings from this study and its feasibility of increasing the capacity of layered oxide cathodes through high-voltage cycling is evaluated though the high voltage long-term cycling of a pilot-line-fabricated $LiNi_{0.8}Mn_{0.1}Co_{0.1}O_2$–Graphite full pouch cell.

4

2. Results and Discussion

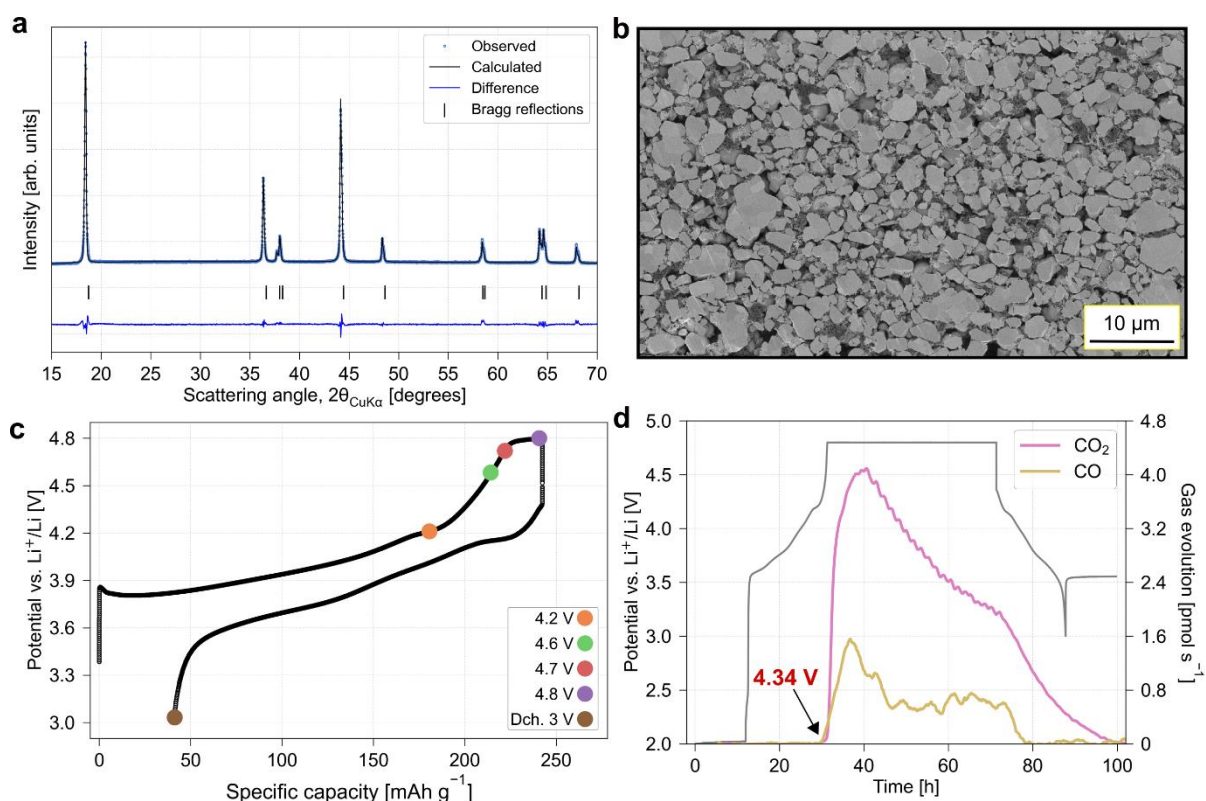## 2.1 Characterisation of the Pristine Material

Figure 2: (a) Powder X-ray diffraction - Rietveld refinement plot of the NMC811 powder. (b) Cross-sectional SEM image of the pristine cathode (c) Potential versus specific capacity plots of NMC811 charged to 4.8 V, and discharged to 3 V. The voltage-cutoffs of the electrode samples characterised ex-situ are also highlighted. (d) OEMS data outlining the onset of gas evolution at 4.34V.

The phase purity of the single crystalline $LiNi_{0.8}Mn_{0.1}Co_{0.1}O_2$ powder, henceforth NMC811, was confirmed through inductively coupled plasma – optical emission spectroscopy (ICP-OES) and X-ray diffraction (XRD). The stoichiometry was determined to be $Li_{1.01}Ni_{0.81}Mn_{0.06}Co_{0.11}O_2$ and Rietveld analysis of the XRD data (Figure 2a) showed that the data could be fitted with a O3-type $R\bar{3}m$ structure model with a Li–Ni inter-site mixing of 1.79(7)% (Table S1 for refined parameters).[32] A cross-sectional scanning electron microscopy (SEM) image outlining the presence of the 3–5 μm single-crystalline particles of the pristine NMC811 cathode is shown in Figure 2b. Note that the cathode is identical to the one used in our previous study.[33] The first galvanostatic charge-discharge profile of a NMC811 half-cell versus Li metal is presented in Figure 2c. Charging to 4.8 V leads to a calculated delithiation of 0.87 mol Li^+ per formula unit, corresponding to a capacity of 242 mAh g^{-1}. Upon discharging to 3 V, a capacity of 202 mAh g^{-1} is obtained, resulting in a Coulombic efficiency of 83.5%. Expectedly, the high cut-off voltage leads to appreciable voltage hysteresis and capacity fade during discharge and larger than typical values obtained when this same sample is cycled to only 4.2 V.[34,35] Previously, NMC811 has been reported to delithiate via a solid-solution mechanism, with an O3 to O1 phase transformation only occurring with an extended high-voltage hold at high temperatures (60 °C).[36] Thus, a significant

5

proportion of the degradation in the *ex-situ* samples occurs due to CO_2 and CO evolution after 4.34 V as evidenced by the on-line electrochemical mass spectrometry data (OEMS) shown in Figure 2d. Gas evolution occurs due to electrode side reactions with ethylene carbonate (EC), the result of which is an O deficient surface which densifies into a rock salt phase upon discharge.[37,38] Nevertheless, the hysteresis observed for NMC811 is still comparatively lower than that of $LiCoO_2$ (Figure S1) and Li-rich Ni-Mn-Co (NMC) oxides charged to the same voltage.[28,39] Thus, to investigate the link between charge compensation and this high voltage degradation, X-ray spectroscopy measurements were carried out on cathodes ex situ, after being charged to the voltages highlighted in Figure 2c.

2.2 Transition metal versus Oxygen Redox

### 2.2.1 Transition metal K-edges plateau beyond 4.2 V (vs. Li$^+$/Li)
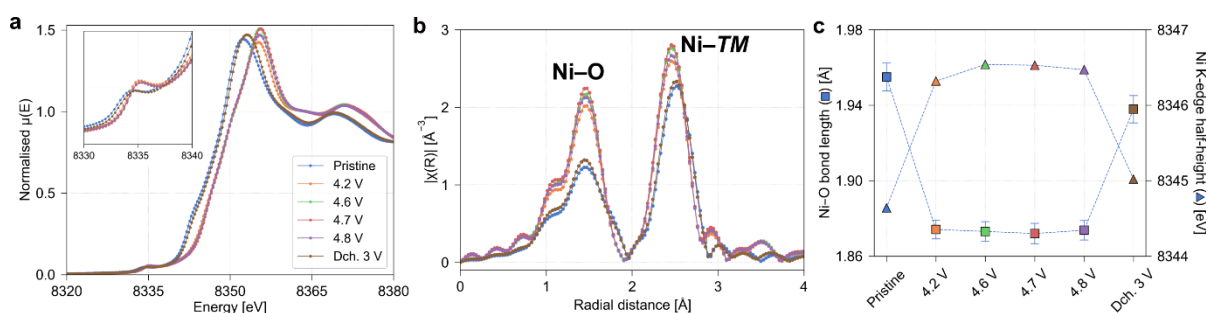
Figure 3: (a) Ex situ Ni K-edge XANES data, with a magnified view of the pre-edge in the top left. μ(E) is the absorption coefficient. Dch. denotes discharge. (b) The corresponding Fourier-transformed χ(R) space - extended x-ray absorption fine structure (EXAFS) data. The first and second coordination shells are annotated. (c) The first coordination shell Ni–O bond length obtained from fitting the EXAFS data, and the Ni K-edge half-height. Note that the legend in the left panel applies to (b), and (c).

The role of *TM* and O in the charge compensation process during delithiation was investigated using multiple X-ray spectroscopic techniques. In addition to examining different facets of the electronic structure evolution, combining these techniques facilitates the deconvolution of bulk and surface regions due to their different probe depths. The Ni K-edge transmission XAS data, focussing on the X-ray absorption near-edge structure (XANES) region, is presented in Figure 3a and corresponding data from the Mn and Co edges are shown in Figure S2. The Ni spectral data reveals a uniform shift towards higher X-ray energies with an unchanged edge line-shape during charge, before returning close to its original state upon discharge. This shift is usually tracked using the edge half height, i.e., the X-ray energy where normalised intensity equals 0.5. In contrast, Mn and Co edges exhibit changes in the line-shape without a continuous edge shift. Interestingly, all three *TM*s show negligible spectral changes between 4.2 and 4.8 V. This trend is also visible in the corresponding pre-edge data, which, based on the comparable pre-edge intensities across the samples, do not provide any evidence for *TM* migration into tetrahedral sites. The extended X-ray absorption fine structure (EXAFS) data, shown in Figure 3b, also shows clear reversible changes for Ni during cycling, and largely reflect the same trends as the XANES data. For a single Ni–O_6 octahedron, a linear relationship is expected between the Ni–O bond length and a changing formal Ni oxidation state.[40] However, contrary to expectation, the Ni–O distances appear to plateau during charge beyond 4.2 V prior to returning to close to the pristine state upon

6

discharge (Figure 3c), thereby conforming to the trends in the XANES data. This non-linear evolution shows that for delithiated NMC811 cathodes, bulk oxidation reactions that result in changes to the first coordination shell of Ni, reach a steady state at 4.2 V, at an approximate delithiation of 0.66 mol Li$^+$ per formula unit. The Co–O and Mn–O bond lengths also exhibit identical plateauing behaviour (Figure S2). Similar trends are also observed for LiCoO$_2$ (LCO), although poorer reversibility is observed upon discharge (Figure S3). This steady-state behaviour is similar to that observed at 4.5 V in Li- and Mn-rich layered oxide cathodes and is often described as the end of *TM* oxidation and the beginning of discrete O oxidation.[39] Therefore, in NMC811 and LCO, it would be rational to propose that O only begins to participate in the charge compensation mechanism after 4.2 V i.e., where the TM K-edge evolution ceases and the *TM*–O bond length plateaus. However, as was alluded to in the introduction, such an ionic description does not represent the electronic charge compensation in such late-3d-*TM* containing layered oxide cathodes as it downplays the role of orbital covalency and ligand-to-metal electron sharing. This will be experimentally validated in the following sections.

2.2.2 All oxidation is driven by O hole formation
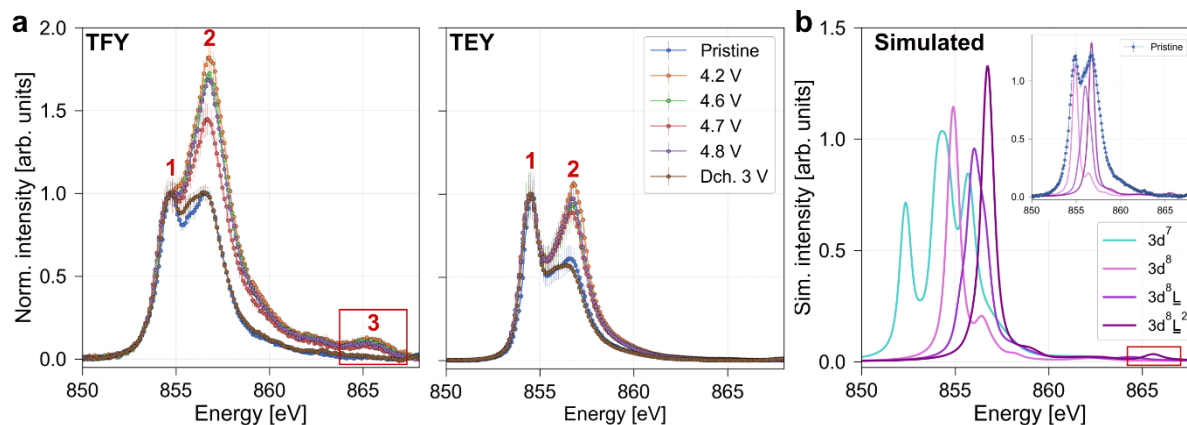
Figure 4: (a) Background-subtracted, normalised Ni L$_3$-edge spectra of NMC811 collected in total fluorescent (TFY) and electron (TEY) yield modes. The three main features in the experimental spectra are labelled 1, 2 and 3. (b) Simulation of Ni L$_3$-edge spectra of a Ni–O$_6$ octahedron. The inset compares the pristine NMC811 TFY data with simulations for the $|3d^8\rangle$, $|3d^8\underline{L}\rangle$ and $|3d^8\underline{L}^2\rangle$ electronic states.

For a more sensitive electronic and sample-depth-dependent probe of the redox-active valence orbitals, Ni L$_3$-edge XAS data was collected in total fluorescence and electron yield modes (TFY and TEY, respectively). The TFY and TEY modes enables depth-profiling of the cathodes with approximate probe depths of 100–200 and 0–10 nm, respectively.[41] This is critical for a thorough characterisation of the Ni-rich layered oxide cathodes as they have been previously shown to exhibit depth-dependent changes in the electronic structures of the TM species.[42,43] The single-crystalline morphology of the cathode particles used in this work helps to prevent high-voltage intergranular cracking,[44] thereby minimising the formation of extraneous surface species.[45] The experimental TFY and TEY data, presented in Figure 4a, are the average of three background-subtracted scans normalised to the peak at ≈855 eV (denoted as 1). To aid the interpretation of the experimental data, Ni L$_3$-edge XAS spectra were also simulated using a single Ni–O$_6$ cluster (Figure 4b). In NMC811, simple electron counting places the majority of Ni in the +3 formal oxidation state. However, the simulated $|3d^7\rangle$ spectrum clearly does not match

7

experimental data. Instead, a mixture of the $|3d^8\rangle$, $|3d^8\underline{L}\rangle$ and $|3d^8\underline{L}^2\rangle$ states suitably describe the pristine NMC811 sample (Figure 4b inset). This indicates that O holes are already present in the pristine material, which conforms to previous studies outlining the ligand-dominated ground state of $LiNiO_2$.[7,9] Thus, the oxidative changes in both experimental data , namely to the ≈857-eV feature (denoted as 2), is ascribed to the enhancement of the $|3d^8\underline{L}\rangle$ and $|3d^8\underline{L}^2\rangle$ line shapes. Further proof is obtained from the broad feature at ≈867 eV (denoted as 3), which appears to originate from the $|3d^8\underline{L}^2\rangle$ electronic configuration as per the simulated data (highlighted in the red box). The same feature is seen in the TFY data of the charged samples, confirming that delithiation is compensated through O hole formation. Moreover, no visible shift to higher binding energies is observed in the experimental data, implying negligible contribution of Ni to charge compensation, as would be expected for a material that does not contain any formal $|3d^7\rangle$ Ni^{3+} to begin with. Interestingly, this is not replicated in the Co L_3-edge data and weak shifts to higher energy are observed (Figure S4). Owing to its lower effective nuclear charge, Co cations are less electronegative than equally charged Ni cations. Thus, an expectedly weaker O contribution is observed for the Co-centred octahedra of NMC811 (Figure S4).[4] This same behaviour is also observed in LCO (Figure S5) and would contextualise its comparatively high stability with respect to gas evolution.[46,47] Like the *TM* K-edge data, the L-edge data also shows reversibility upon discharge, despite the high charging cut-off voltage. As before, the NMC811 sample shows significantly better reversibility than LCO.

As is evident from Figure 4a, the NMC811 cathodes show different bulk and surface reactivities, which has significant ramifications for delithiation kinetics. In the pristine sample, Ni TEY data indicates a more reduced surface, revealing the inherent thermodynamic instability of the ligand hole-containing octahedra that are needed to maintain charge neutrality. During delithiation, the TEY data follows the same trends as the TFY data, albeit to a lower extent because of the more reduced starting point. Interestingly, even at high voltages, hole density at the surface does not appear to exceed that which is observed in the pristine bulk. Furthermore, the ≈867-eV feature (denoted as 3) is noticeably absent in the surface sensitive TEY data and further emphasises the high reactivity of these sites. Together, this allows previously reported surface reduction and rock-salt layer formation (via electrolyte side-reactions) to be attributed to reactions involving these ligand hole-containing octahedra.[48] A similar surface-to-bulk oxidation state gradient was observed in the Co L-edge data, with the surface appearing more reduced compared to the bulk (Figure S4). Thus, with the modal Ni environment evidently possessing significant quantities of O-holes in the pristine, charged and discharged samples, O K-edge XAS and RIXS measurements were performed to investigate the possible formation of side-products of O oxidation (for example, the O–O dimers as discussed for Li-rich materials).

2.2.3 Oxygen K-edge evolution *also* plateaus beyond 4.2 V (vs. Li⁺/Li)

Changes in the O electronic structure during cycling were investigated through O K-edge soft XAS. The pre-edge in the O K-edge XAS data (≈530 eV) is sensitive to hybridised O 2p – TM 3d orbitals located in the sub-surface (100–200 nm) region. As seen in Figure 5a, the intensity of the pre-edge increases upon charging to 4.2 V, indicating the creation of holes in TM–O hybridised states, an increase in TM–O covalency, or both. Additionally, the O K-edge (535–538 eV, along the 0.5 intensity marker), moves

8

towards higher energies. Surprisingly, like the *TM* K- and L-edges, this evolution plateaus and shows negligible changes between 4.2 and 4.8 V, before returning to a state close to the pristine material upon discharging. This indicates that the same electronic steady state is also reached after 4.2 V for O in the bulk of NMC811. Furthermore, unlike Li-rich NMC cathodes, no new features close to the pre-edge at ≈531 eV, are visible between 4.2 and 4.8 V, even when the spectra are plotted normalised to the pre-peak intensity maximum (Figure S6). Interestingly, surface-sensitive TEY O K-edge data (Figure 5b), exhibits a continuous evolution of the pre-edge intensity during charge. This, in combination with the changing line shape and non-linear progression of the edge position, is indicative of an oxidised surficial O environment occurring at high voltages. Despite the remarkable reversibility observed during discharge, a direct interpretation of the TEY data is complicated by changes induced following electrode–electrolyte side reactions and gas evolution, as outlined previously (Figure 2d). Similar behaviour is also seen in the TFY O K-edge XAS data of the LCO (Figure S7). In LCO, additional features do form in the pre-edge during charging, which have been previously attributed to Co–O rehybridisation due to local distortions of the Co–O bond arising due to bulk phase transformations.[49] Nevertheless, in both NMC811 and LCO, the same trends are observed in the TM and O XAS data during charging. This reaffirms the invalidity of separating *TM* and O contribution to charge compensation in covalent systems – when hybridised, the same trends will be observed in both.
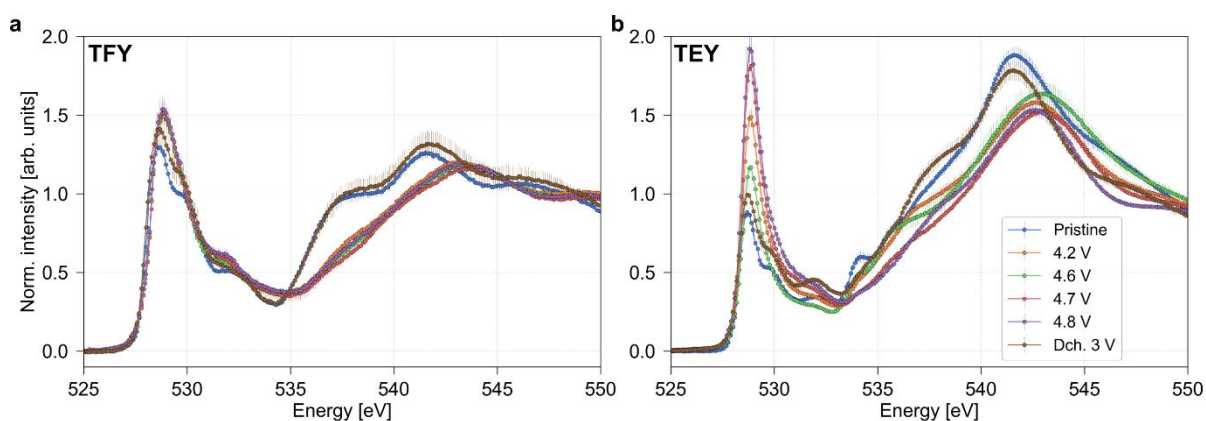

Figure 5: Background-subtracted, normalised O K-edge data obtained from the NMC811 electrodes collected in the (a) TFY and (b) TEY modes.

2.2.4 Growth in the RIXS features from 4.2 to 4.8 V

To obtain greater selectivity and to deconvolute the species obfuscated by pre-edge intensity in the O K-edge, high-resolution O K-edge RIXS experiments were performed between 527.5 and 533 eV, with the resultant RIXS maps shown in Figure S8. Following this, RIXS scans were collected at 531.3 eV from 10 different sample locations, the average of which are shown in Figure 6. Here, three new spectral features at 0–2, 5 and 8 eV energy loss are observed during charging. and are comparable to those observed in Li-rich cathodes.[28] Unlike the spectroscopy data presented thus far, it is evident that these features become noticeably more intense in the 4.6, 4.7 and 4.8 V samples. Note that the 4.7-V sample, like in the Ni L-edge spectra, breaks this increasing trend; this is most likely an isolated sample-dependent issue and so, quantification or inference of the RIXS feature based on spectral weight was

not carried out. It is also worth noting that inhomogeneities in the probed cathode area can also affect the spectral intensity and complicate analyses that are based on the spectra alone. Unlike the other features, the 5-eV feature shows no visible growth upon charging from 4.2 to 4.8 V. The origin of this feature, also observed in delithiated LiNiO$_2$,[31] is currently unclear and may be linked to TM–O hybridised states based on their resemblance to the evolution of the Ni L-edge XAS data (Figure 4b).
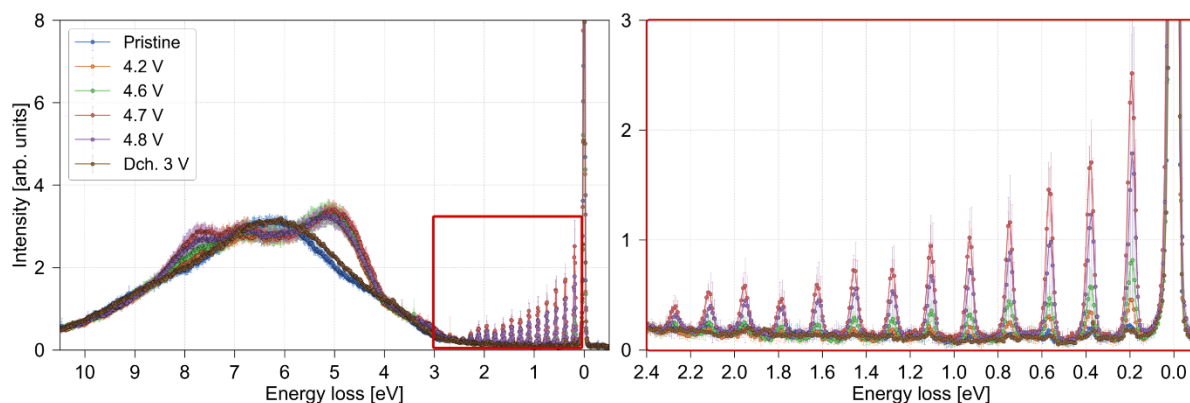

Figure 6: RIXS spectra of the NMC811 electrodes collected at ≈531.3 eV incident X-ray energy. The vibronic features (0–2 eV) are magnified in the right panel.

As mentioned earlier, NMC811 is widely shown to maintain its bulk crystallographic structure within this voltage window.[36] However, redox dynamics are influenced by multiple competing factors such as pristine structure, chemical composition, and morphology. Therefore, two additional materials, LCO and Li$_{1.2}$Mn$_{0.54}$Ni$_{0.13}$Co$_{0.13}$O$_2$ (Li-rich NMC), each with drastically different delithiation pathways, were also investigated.[50] [28]

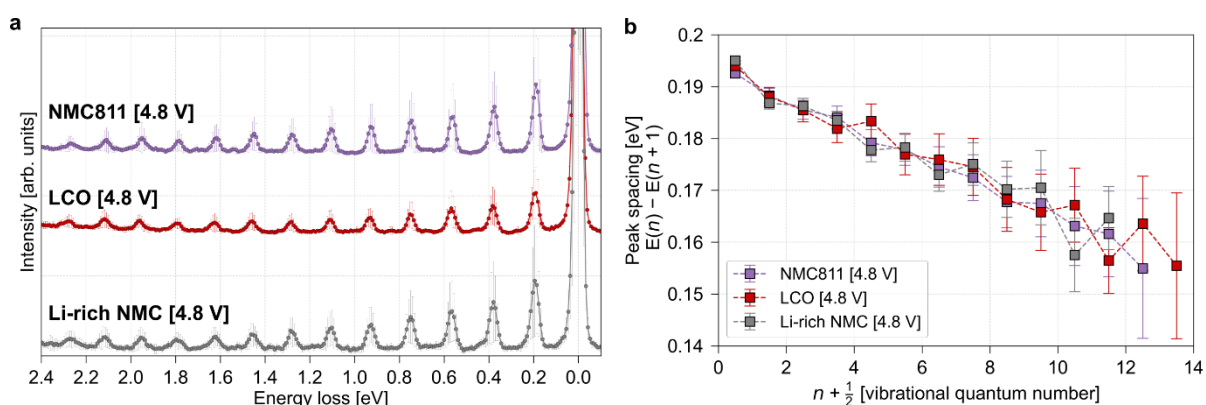## 2.2.5 Structural delithiation pathway does not influence the RIXS feature

Figure 7: (a) The vibronic features measured at 4.8 V in charged NMC811, LiCoO$_2$ (LCO), and Li$_{1.2}$Mn$_{0.54}$Ni$_{0.13}$Co$_{0.13}$O$_2$ (Li-rich NMC) cathodes. (b) Peak spacing of the vibronic features plotted as a function of the vibrational quantum number, n, for the cathode materials at 4.8 V.

Figure 7a compares the RIXS spectra of NMC811, LCO and Li-rich NMC cathodes at 4.8V vs. Li$^+$/Li. Despite their drastically different crystallographic responses to delithiation, state of charge, and

10

alleged O-redox properties, it is evident that they possess a common characteristic that gives rise to this feature. This is also true for $LiNiO_2$ and $LiNi_{0.98}W_{0.02}O_2$ cathodes, as reported previously.[29,31] To validate the commonality of the 0–2 eV energy loss feature for each 4.8V sample, the peak-spacings of the vibronic features were plotted against vibrational quantum numbers in Figure 7b. All other samples are shown in Figure S9. The peak-spacings measured for the NMC811, LCO and Li-rich NMC cathodes expectedly decreased in accordance with the energy levels of anharmonic potential well. Together with literature reports, the peak spacings resemble the vibrational energy levels of the electronic $^3\Sigma_g^-$ ground state of molecular O_2.[28,51] Although previous high-efficiency (but lower resolution) RIXS studies of delithiated LCO have showed comparable CT features, some studies that utilise bulk sensitive techniques e.g. neutron diffraction also argue against O dimerisation in LCO at highly delithiated states.[50,52] Furthermore, considering that the pristine, 4.2 V and discharged NMC811 RIXS data show weak vibronic spectral features (Figure S10), the statistical analysis was performed using functional principal component analysis (FPCA). Upon imposing a data variance threshold >80% in accordance with the literature,[53] FPCA confirms that the weak vibronic RIXS features observed in the pristine, 4.2 V charged, and 3.0 V discharged samples are statistically robust and represent real data within the 84.94%, 85.33%, and 90.12% data variance, respectively. The observation of these features in the pristine and discharged samples strongly questions the proposed mechanisms by which O–O dimers are believed to form. Furthermore, the vibronic features are observed well-below the gas evolution onset potential of NMC811 (4.34 V, Figure 2d) and provides compelling support for the assertion that the features themselves are not linked to gas evolution from the bulk of the cathode. Therefore, using RIXS to ascertain the role of O–O dimerisation in the bulk charge compensation mechanism and its ability to provide 'excess' capacity necessitates additional scrutiny, especially when considering the difficulty in separating it from possible surface contributions.[10,54]

## 2.5 Long-term high-voltage cycling of NMC811–Graphite pouch cells

Typically, high-voltage O-redox activity is thought to be intimately linked with bulk structural transitions. In Li-rich NMC cathodes, these changes are irreversible, leading to poor long-term electrochemical performance. Considering the evident O-redox activity, gas evolution and RIXS features exhibited by NMC811, the possibility of increasing its specific capacity through high-voltage operation was investigated in a NMC811–Graphite pouch cells, cycled under practically relevant conditions. In our previous work, it was shown NMC811–Graphite full cells are capable of operating in a wide operating voltage window of 2.5–4.4 V for over 100 cycles with less than 10% capacity fade.[33] Based on the results in section 2.2.1, at 4.4 V, the cathode is understood to be operating within the steady-state regime where O K-edge RIXS features are present, similar to what was observed at 4.2 V (vs. Li+/Li). This is illustrated through *operando* EXAFS studies of the pouch cells cycled under the same conditions (Figure S11).
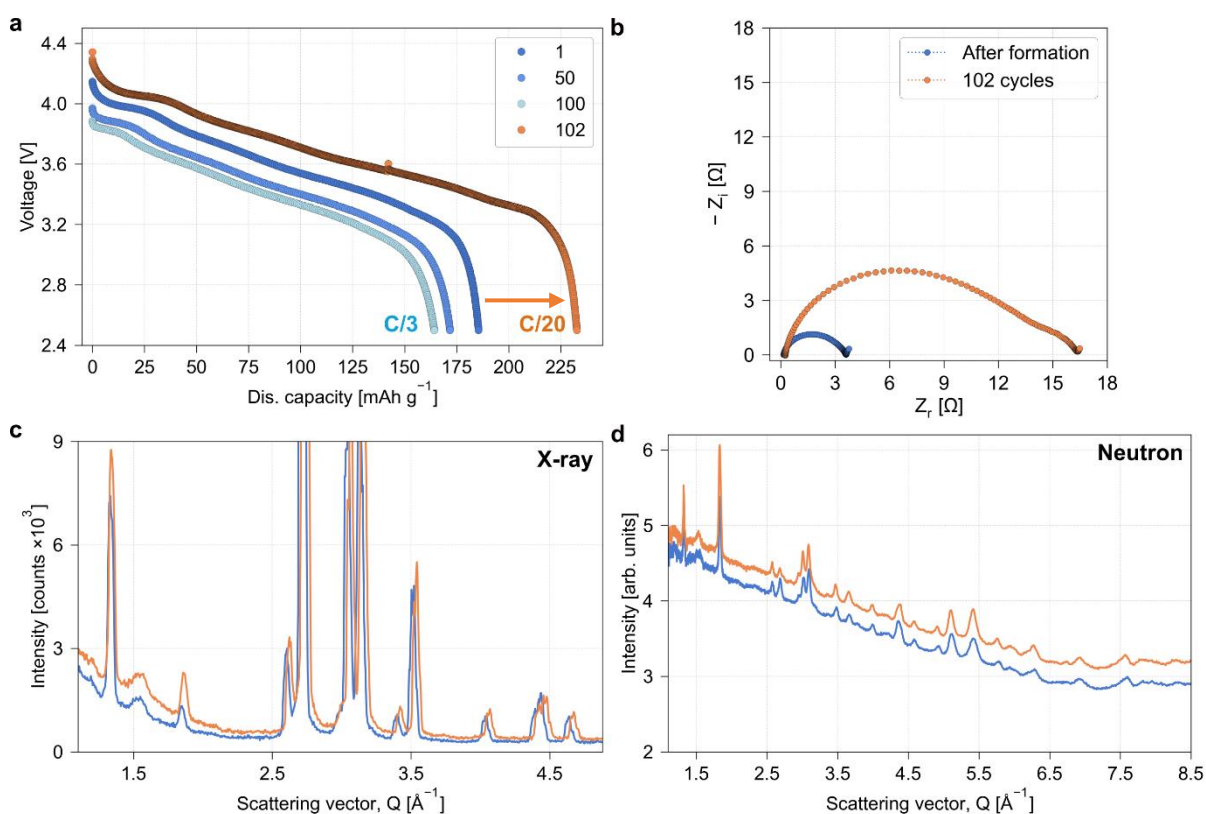
Figure 8: (a) Voltage vs discharge capacity plot for NMC811–Graphite pouch cells cycled between 2.5 – 4.4V. Cycles 1, 50 and 100 were cycled at C/3; cycle 102, illustrating the kinetic origin of the capacity fade, was cycled at C/20. (b) Electrochemical impedance spectroscopy (EIS) data of the after-formation and 102nd cycled cells. X-ray (c) and neutron diffraction (d) data from the NMC811–Graphite pouch cell in the discharged state after-formation and 102 cycles.

This cycling regime leads to capacity fade and impedance growth over 100 cycles (Figure 8a and 8b). The capacity loss observed here is predominantly of kinetic origins as illustrated by the increased capacity during the diagnostic C/20 cycle. However, despite operating in a plateau/steady-state regime (i.e., > 4.2 V), no significant bulk structural changes are observed after 100 cycles. This is

based on the similarities in the *in-situ* X-ray and neutron diffraction data collected on discharged pouch cells after formation and 102 cycles (Figure 8c and 8d). The presence of voids in the cathode bulk, similar to measurements performed for Li-rich cathodes, was investigated using operando small-angle X-ray scattering (SAXS).[55] Previously, it was shown that upon charging, Li-rich cathodes display a reversible growth of a feature centred at ≈0.4 Å^{-1}, which was attributed to *TM*-migration-induced formation of vacancy clusters/voids of decreased electron density. This feature was seen to grow in intensity with continued cycling. For NMC811, this is feature is not observed to any appreciable degree in either early- or late-stage cycling (Figure 9a and 9b, respectively).
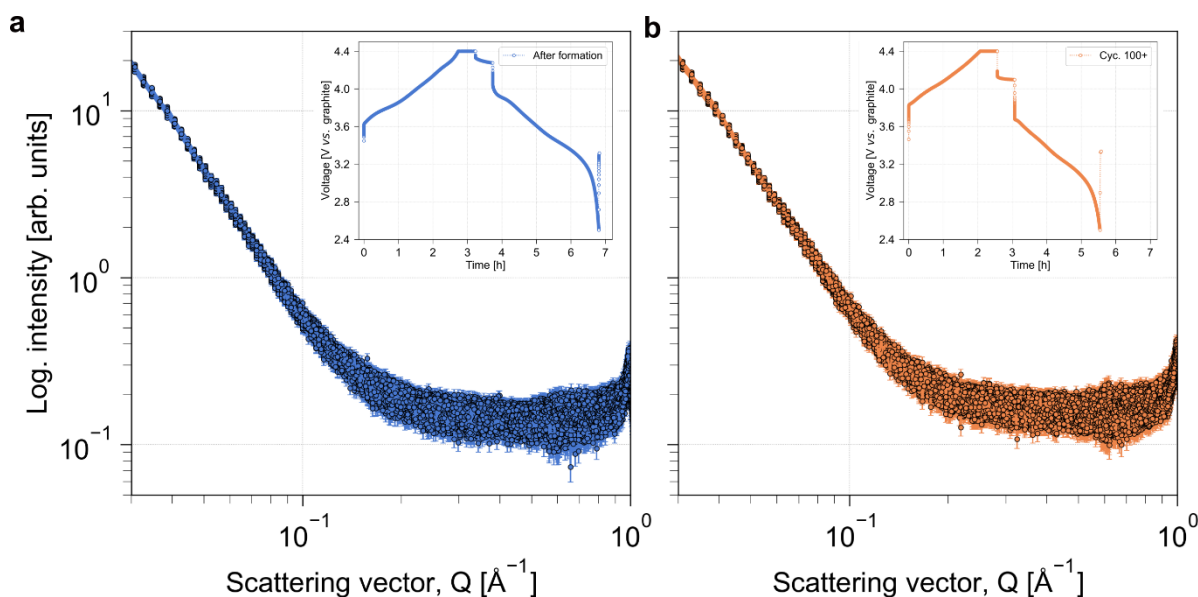
Figure 9: Operando small angle X-ray scattering (SAXS) of a NMC811–graphite pouch cell cycled (a) after-formation and during the (b) 102nd cycle. The electrochemical profiles are shown in the inset.

Taken together, these results highlight the robustness of NMC811 in undergoing reversible bulk (de-)lithiation under high-voltage conditions. However, as implied by the Ni L- and O K-edge TEY data, significant changes occur at the surface, presenting a challenge for long-duration performance. Thus, if these cathodes were to operate at such high voltages under industrially relevant conditions, the associated degradation must be mitigated through electrolyte engineering or cathode surface passivation. There is no evidence to suggest that bulk O-redox, i.e., ligand hole formation in NMC811 cathodes, affects their ability to reversibly cycle Li$^+$. However, reactive sites formed at the particle surface can promote harmful side reactions, leading to significant gas evolution and cathode surface reconstruction. We attribute reactive surface O to this phenomenon, acting as the leading cause of cell impedance, that itself drives the kinetically limited performance fade.

3. Conclusions and Outlook

The aim of investigating charge-compensating redox mechanisms in Li-ion battery cathodes is to enhance specific capacity while preserving cycling stability during higher states of delithiation. Recent studies suggest a need to reassess conventional ionic descriptions of charge compensation mechanisms in common Li-ion layered oxide cathodes. This study uses commercial single crystalline $LiNi_{0.8}Mn_{0.1}Co_{0.1}O_2$ (NMC811) cathodes to explore the charge compensation mechanism via *ex-situ* X-ray spectroscopy. In highly covalent layered oxide cathodes, changes in electron density manifest in the ligands (oxygen anions), leading to an increased proportion of structurally independent $|3d^8\underline{L}\rangle$ and $|3d^8\underline{L}^2\rangle$ electronic configurations. No formal Ni oxidation is observed at any state of delithiation. This contextualises the observation of high-resolution resonant inelastic X-ray scattering (RIXS) features, attributed to O dimerisation, and explains their presence prior to the onset of gas evolution without necessitating bulk void formation. These findings contribute to the growing evidence of widespread O-redox activity in late-*TM*-containing cathodes because of strong TM–O hybridisation and ligand-to-metal electron sharing. When considering that both $LiCoO_2$ and $Li_{1.2}Mn_{0.54}Ni_{0.13}Co_{0.13}O_2$ cathodes also exhibit the same RIXS features upon delithiation, it becomes difficult to ascertain the role of O dimerisation, how closely it is linked to true O-redox activity, and how any specific bulk material property—composition, stoichiometry, pristine structure, or delithiation pathway—controls O dimerisation within them. For NMC811, reversible bulk charge compensation is well-known, but its propagation at the surface differs significantly. Therefore, strategies to passivate the surface, incorporate core-shell morphologies, or adding electrolyte additives can all be used to limit the reaction between oxidised O and the electrolyte. This will enhance the ability of layered oxide cathodes to withstand protracted cycling at elevated voltages, thereby fortifying their long-term cyclability.

14

4. Experimental Details

Materials

The single-crystalline $LiNi_{0.8}Mn_{0.1}Co_{0.1}O_2$ (NMC811) cathode studied here is identical to that in our previous work, Ref. [33], and was supplied by an industrial partner. Complete details may be found in Ref. [33] section IV.

$LiCoO_2$ (LCO) powder was purchased from Sigma-Aldrich (99.8%). $Li_{1.2}Mn_{0.54}Ni_{0.13}Co_{0.13}O_2$ (Li-rich NMC) was synthesised through a coprecipitation reaction. Hydrated Mn, Ni and Co sulfate precursors were dissolved into deoxygenated deionised (DI) water (50 mL) to create a 0.40 mol dm^{-3} sulfate solution. This was added dropwise into a heated (50 °C), stirred (250 rpm), and deoxygenated solution of sodium hydroxide (NaOH, 400 mL, 0.48 mol dm^{-3}). The reaction was left to stir for 4 h under a continuous flow of N_2 gas. The insoluble hydroxide product was then allowed to settle, following which it was filtered. During this process, the powder was washed with copious amounts of DI water and filtered under vacuum using a 1–2 μm pore sized cellulose membrane. The powder was washed until the filtrate was neutral in pH. The residue was dried overnight in an oven at 85 °C. The dried product was ground together with the required amount of Li_2CO_3 with an agate mortar and pestle. This mixture was calcined in a Carbolite™ CWF Chamber Furnace at 900 °C for 24 h, prior to quenching to room temperature. The cooled product was then reground and stored for electrode preparation. See Tables S2 and S3, and Figure S12 for the XRD characterization of the two samples.

Electrochemical cycling of cathodes for *ex situ* studies

The NMC811 cathode was prepared similar to Ref. [33] In brief, the cathode was prepared with a 95.5:2.5:2 mix of the active material (NMC811), PVDF (polyvinylidene difluoride) binder and conductive carbon additive casted onto a 15-μm thick aluminium foil. For electrochemical cycling, electrodes 14.8 mm in diameter were punched. After weighing and drying overnight at 120 °C under vacuum, the electrodes were transferred into an Ar glovebox. Following this, CR2032-type coin cells were constructed with the NMC811 electrodes using Li metal counter electrodes. A combination of Whatman glass microfibre and Celgard 2400 (on the cathode side) separator were used for the cells. The 'LP57' electrolyte was 1 M $LiPF_6$ in ethylene carbonate (EC) – ethyl methyl carbonate (EMC) (3:7 by weight %) with 2% vinylene carbonate (VC) additive (Solvionic), which was thoroughly dried using molecular sieves before cell assembly. Galvanostatic cycling were carried out to the desired voltages using a Biologic BCS cycler. In all cases, the cells were galvanostatically cycled at C/20 rates (1C = 275 mA g^{-1}) with a final constant voltage (current-limited to C/40) hold at the specific voltages to ensure homogeneous delithiation.

For electrochemical testing, LCO and as-synthesised Li-rich NMC were thoroughly mixed with C65 carbon black (Imerys) and polyvinylidene fluoride (PVDF, M_w=534000, Sigma-Aldrich) with a weight ratio of 90:5:5 in an agate mortar inside an Ar-filled glovebox. N-Methyl-2-pyrrolidone (NMP) was added before mixing to form a homogenous slurry, which was cast onto carbon-coated Al foil using a doctor blade with height 150 μm. The slurry was dried at 100 °C for one hour before transfer to an 80 °C vacuum oven overnight. Electrodes of 12 mm were punched from the prepared film and transferred to

https://doi.org/10.26434/chemrxiv-2024-w906n ORCID: https://orcid.org/0009-0006-4979-7980 Content not peer-reviewed by ChemRxiv. License: CC BY-NC-ND 4.0

an Ar-filled glovebox. Coin cells of type CR2032 were assembled using Li metal chips (Cambridge Energy Solutions) as a counter electrode and prepared cathodes as the working electrode. A Whatman glass microfiber separator was wet with 100 μL of 1 M $LiPF_6$ in ethylene carbonate (EC) – ethyl methyl carbonate (EMC) (3:7 wt.%), and an additional Celgard 2400 separator was placed on the cathode side to prevent glass microfiber contamination. The electrolyte was pre-dried using molecular sieves to remove any residual moisture. Galvanostatic charge and discharge tests were collected using an Arbin LBT21084 potentiostat at C/20 for LCO (1C = 140 mA g^{-1} for the 4.2 V sample, and 1C = 220 mA g^{-1} for the 4.8 V and discharged sample) and with a current density of 5 mA g^{-1} for Li-rich NMC. A constant voltage (current-limited to C/40) was also applied at the cut-off voltages.

After cycling, the electrodes were removed from the cells in an Ar-filled glovebox and thoroughly rinsed with DMC (Dimethyl carbonate) before transferring into their respective holders for *ex situ* studies.

Fabrication and electrochemical cycling of NMC811–graphite pouch cells

The fabrication and electrochemical cycling of NMC811-graphite cells were carried out identical to our previous work, Ref. [33]. The cycling process is discussed in brief here. After fabrication, the cells were held at 1.5 V for 20 h at 40 °C to ensure complete electrolyte wetting of the electrodes. Following this, two formation cycles were performed under galvanostatic conditions at approximately C/20 (1C = 200 mAh g^{-1}) rate between 2.5 and 4.4 V at 40 °C. Further galvanostatic cycling was again carried out at 40 °C between 2.5 and 4.4 V using a constant current–constant voltage (CCCV) mode at C/3-rate for 100 cycles. The CV step during charge was controlled using a current value of C/30 as the lower limit. All the cycling was carried out using a Maccor 4000 series cycler. Potentiostatic electrochemical impedance spectroscopy (PEIS) data was measured at 3.8 V at 25 °C, with an amplitude of 10 mV between 100 kHz and 10 mHz after formation and 100 cycles using a Biologic VMP3 potentiostat. For the operando studies after formation and 100 cycles, two pouch cells were used to ensure continuous long-term cycling.

X-ray diffraction (XRD) & cross-sectional scanning electron microscopy (SEM)

XRD and SEM data were collected identical to Ref. [33], which contains further details about the same. In brief, XRD measurements of the pristine NMC811, LCO and Li-rich NMC powders were performed using a Malvern Panalytical Aeris diffractometer (40 kV, 15 mA) with non-monochromated CuKα radiation. Data was collected in reflection mode between an angular range of 10–75° (2θ) with a step size of ≈0.01° and time per step of ≈150 s, using a PIXcel1D-Medipix3 detector. A zero background Si holder (spun during the measurement) was used. Rietveld[56,57] analysis of the XRD data was performed using TOPAS-Academic (v7) software.[58] In the refinement of the NMC811 powder, the $R\bar{3}m$ unit cell parameters, the scale factor, z coordinate of the oxygen atom, and the occupancies Li and Ni atoms were allowed to refine. The occupancies of the Mn and Co were fixed to values obtained from ICP-OES analysis. Similarly, the isotropic atomic displacement parameter was fixed to 0.5 in all cases and not refined. For the commercial LCO and as-synthesised Li-rich NMC data, only a Pawley (unit cell) [59] refinement was performed considering the superstructure reflections. Definitions of the various

16

refinement functions and metrics can be found in the Topas manual. The refined values are included in the SI.

Cross sections for SEM of the pristine cathode were prepared by Ar broad-beam ion milling (BBIM). Images were obtained using settings of 2 kV and 100 pA.

Inductively coupled plasma optical emission spectroscopy (ICP-OES)

Elemental composition of the NMC811 powder was determined using an Agilent 5110 inductively coupled plasma optical emission spectrometer. For the measurement, 50 mg of material was dissolved in a 5 mL mixture of ultra-trace pure 37% HCl and 65% HNO3 (3:1 v/v). In triplicate, the sample were heated to 115 °C for 45 min. on a DigiPREP hot block (QMX Laboratories, UK). Prior to analysis, sample solutions underwent a 1000x dilution with a 5% HNO_3 matrix.

Online electrochemical mass spectroscopy (OEMS)

OEMS data was measured using a continuous flow system set-up passing through an electrochemical cell head space to the quadrupole mass spectrometer (Pfeifer, Thermostar), described in detail elsewhere.[37,38,60] Measurements were done in coin cells where the top case has a 0.23 mm perforation for gas release, encased inside a 1" Swagelok-type cell. The cells were assembled inside an Ar-filled glove box in half-cell configuration with a 15.6 mm diameter Li chip (thickness 0.25 mm, LTS Research Laboratories) reference/counter electrode, 12.7 mm diameter cathode coated on Al foil and 17 mm Celgard separator soaked in 75 µL of LP57 electrolyte containing 2% VC. The cells were then attached to the OEMS set-up without exposing them to ambient air via quick-connect joints. The cells were galvanostatically charged to 4.8 V at C/20 and held there for 40 h before discharging to 3.0 V. Before and after cycling, the cells were held for 12 h at OCV to collect sufficient background to minimize signal drift during the measurement.

***TM* K-edge X-ray absorption spectroscopy (XAS)**

Ex situ XAS data of the electrodes were collected on the B18 Core-XAS beamline at the Diamond Light Source, Oxford, UK.[61] For the measurements, the electrodes were sealed in Kapton tape inside the glovebox before loading onto the custom-made sample holder at the beamline. All measurements were carried out in transmission mode under ambient conditions using the Pt-coated branch of collimating and focusing mirrors with a Si 111 double-crystal monochromator. A step size of 0.3 eV was used for all measurements. For every sample, at least three spectra were collected and then merged.

Operando measurements were also performed under identical conditions using a Biologic SP150 potentiostat. For each cell, two spots were measured for statistical confidence. Electrochemical cycling was performed galvanostatically between 2.5 and 4.4 V at C/3-rate. Each cycle consisted of 4 steps: (1) charge to 4.4 V, (2) 30-min constant-voltage hold, (3) 30-min rest (I = 0 mA), and (4) discharge to 2.5 V.

Reference spectra from corresponding metallic foils were also simultaneously used for energy calibration. The subsequent pre-edge background subtraction and post-edge normalisation were

performed with Athena software.[62] A Python script based on the Larch library[63] was used for modelling the Ni, Co, and Mn K-edges' Fourier-transformed (FT) extended X-ray absorption fine structure (EXAFS) spectra. The structural models for NMC811 and LCO were obtained from the literature. Using this, the list of scattering paths was created through the feff61 function.[64] The single scattering paths corresponding to the first and second coordination shells surrounding the TM ions were used for the modelling of EXAFS spectra using the Feffit function from the Larch library. Four EXAFS parameters such as amplitude reduction factor (S02), Fermi energy (E_0), bond length (r), and Debye-Waller factor (σ^2) were employed for the data modelling. The S02 and E_0 parameters were constrained to be the same for each scattering path and refined during the modelling. The r and σ^2 parameters were varied without any constraint for both scattering paths. The modelling results were assessed based on the R-factor and χ^2 values (Table S4). For ex situ NMC811 samples, k-ranges of EXAFS data used for Fourier transformation were 3.1–13.2, 3.1–11.2, and 3.1–10.5 Å^{-1} for Ni, Co and Mn K-edges, respectively. For LCO, k-range used at Co K-edge was 3.2–11.1 Å^{-1}. In case of operando EXAFS data analysis, k-ranges used for were 3.0–11.0, 3.1–10.6, and 3.1 – 9.7, for Ni, Co and Mn, respectively. For all EXAFS modelling, the r-space was chosen to be in the range of 1.0–3.0 Å. The mathematical definitions of R-factor and χ^2 are found in the software manual.

Soft X-ray absorption spectroscopy & Resonant inelastic X-ray scattering (RIXS)

TM L-edge and O K-edge Soft XAS, and high-resolution RIXS experiments were carried out on the I21 beamline,[65] at the Diamond Light Source, similar to our previous study.[29] Measurements were performed at 20 K with continuous beam rastering under ultra-high vacuum conditions on electrode samples loaded on to the sample measurement pucks. XAS data were obtained in total fluorescence and electron yield modes at the Ni, Mn, Co L- and O K-edges. The incident X-ray energy was calibrated relative to the O K-edge pre(-edge) peak of NiO powder and was approximately −0.94 eV. O K-edge data were processed, i.e., background subtraction and normalisation, using the Athena software.[62] For the *TM* L-edge data, the background subtraction was done using a baseline manually created by the interpolation of selected background points. In all cases, the XAS data presented is an average of multiple individual scans.

For the O K-edge RIXS measurements, spectral maps were collected between excitation energies of 527.5 and 533 eV with incremental steps of 0.25 eV for 60 s each. The beam was moved 0.01 mm for every measurement. Following this, 10 individual scans were collected at ≈531.3 eV for 120 s on a fresh spot with continuous shifts of 0.01 mm. Data calibration was performed by measuring a carbon tape after every spectrum. To check the effects of resonance, scans were also collected in identical manner at a lower incident energy (≈531 eV) on the highest charged NMC811 sample. The effect of beam damage was investigated by collecting multiple RIXS scans at ≈531.3 eV on the same spot (without beam rastering). The raw data was processed using DAWN software[66] using established procedures at the beamline. The line scan data presented are an average of 10 scans. Peak Spacing of the 0–2-eV vibronic features were obtained by fitting Gaussian peaks to the data post background subtraction using OriginPro 2022.

Ni L-edge X-ray simulations

For the simulations, a parameterised model was constructed of a single NiO_6 octahedron (O_h point group), that contained Ni 2p, Ni 3d, and ligand orbitals. The ligand orbitals were defined as linear combinations of oxygen 2p Wannier-orbitals as described in Ref. [67]. The model Hamiltonian consisted of the Coulomb repulsion between (1) two Ni 3d electrons (including all multiplet effects), (2) a Ni 2p core and 3d valence electron (including all multiplet effects), (3) Spin orbit interaction in Ni 3d and Ni 2p core level, (4) the onsite energy of the Ni 2p core orbitals, (5) the orbital dependent onsite energy of the Ni 3d valence and ligand orbitals, and (6) the hybridisation strength between the Ni 3d and ligand orbitals. Using this Hamiltonian, XAS excitation was calculated using QUANTY which calculates spectra implemented the Green's function under the dipole approximation.[68] The model contained Coulomb interactions, on-site energies, spin orbit interactions, and hopping integrals as variables. A charge transfer energy (Δ) of 4.2 eV for the d^7 and d^8 states was selected while using −1.2 eV and −2.6 eV for the $d^8\underline{L}$ and $d^8\underline{L}^2$ ($\underline{L}$ is a ligand hole) states, respectively. The d^7 states were stabilised in $d8^{\underline{L}}$ with Δ = −1.2 eV. Thereon, an extra ligand electron was added and Δ increased to avoid charge sharing stabilising into the d^8 states. To account for the extra electron added in the previous simulation, count of ligand electrons in a subsequent simulation was reduced starting from the $d^8\underline{L}$ state, obtaining the $d^8\underline{L}^2$ ground state with Δ = −2.6 eV. The energies of the simulated datasets have been offset by +1.9 eV to match the experimental data. The input file for the simulations is included in the SI.

Functional principal component analysis (FPCA) of RIXS data

FPCA was used to reduce the data noise and produce statistically robust data presentations by creating factors (functions) of the functional variance matrix that maximize the variance. An in-house Python script was used for the analysis. Only data between the (energy loss) range −1 to 2.5 eV, corresponding to the vibrionic RIXS features, were used. The FPCS methodology as well as the scripts used for the same are attached in the SI.

X-ray and neutron diffraction measurements of pouch cells

XRD patterns of the discharged pouch cells after formation and 102 cycles were collected on a Malvern Panalytical Empyrean diffractometer (60 kV, 40 mA) with MoKα radiation in transmission. During the measurement, the pouch cell was fixed onto a holder attached to an XYZ stage. A Zr CuKβ filter, a Soller slit (0.02 rad), a divergence slit (0.5°), and an anti-scatter slit (0.25°) was used on the incident-beam side. Additionally, Anti-scatter (5 mm) and Soller (0.02 rad) slits were used on the diffracted-beam side. Data were collected between 7–32° with steps of ~0.029° (2θ) with a counting time of ≈2400 s per step (≈2 h total time) using a GaliPIX3D detector.

Neutron diffraction data were collected at the ISIS Neutron and Muon Source (Rutherford Appleton Laboratory, United Kingdom) using the Polaris time-of-flight diffractometer.[69] The unmodified (and undeuterated) cell was mounted onto the instrument's standard candle-stick using a multi-purpose sample holder. As the cell was mounted with the pouch's flat surface perpendicular to the incident beam, only data from one of the forward (bank 3, 40.4°–66.4°) and back (bank 5, 134.6°–167.4°) banks were

19

used. Each cell was measured for approximately four hours at the source's current rate at the time of experiment.

The magnitude of the scattering vector (Q) is given by $4 \cdot \pi \cdot \sin(\theta)/\lambda$, where 2θ is the angle between the incident and scattered X-rays and λ is the wavelength of the incident X-rays. Q is related to the interplanar distance (d), as $Q = 2\pi/d$.

Operando Small-angle X-ray scattering (SAXS)

Operando SAXS data of the pouch cells were measured using a Xenocs Xeuss 2.0 instrument equipped with a micro-focus CuKα source collimated with scatter-less slits. Data was measured using a Pilatus 300k detector with a pixel size of 0.172 mm × 0.172 mm. The distance between the detector and the sample was calibrated to be 354(2) mm using silver behenate ($AgOOC(CH_2)_{20}CH_3$). Azimuthal integration of the 2D scattering profile was performed using Xenocs XSACT software and the resulting 1D data corrected for the absorption, sample thickness and background. Cells were cycled using a Biologic SP150e potentiostat. *Operando* data were simultaneously collected for a duration of 120 s. This also included a 0.1 s collection with the beam stop removed to measure the transmission through the cell. This was used for the absorption and background corrections of all the SAXS data. The cycling protocol was identical to that in the EXAFS study.

4. Acknowledgements

5. Declaration of Interests

The authors declare no competing interests.

6. References

1. Páez Fajardo, G.J., Fiamegkou, E., Gott, J.A., Wang, H., Temprano, I., Seymour, I.D., Ogley, M.J.W., Menon, A.S., Stephens, I.E.L., Ans, M., et al. (2023). Synergistic Degradation Mechanism in Single Crystal Ni-Rich NMC//Graphite Cells. ACS Energy Letters, 5025-5031. 10.1021/acsenergylett.3c01596.

2. Zhang, H., Liu, H., Piper, L.F.J., Whittingham, M.S., and Zhou, G. (2022). Oxygen Loss in Layered Oxide Cathodes for Li-Ion Batteries: Mechanisms, Effects, and Mitigation. Chemical Reviews *122*, 5641-5681. 10.1021/acs.chemrev.1c00327.

3. Manthiram, A. (2020). A reflection on lithium-ion battery cathode chemistry. Nat Commun *11*, 1550. 10.1038/s41467-020-15355-0.

4. Kleiner, K., Murray, C.A., Grosu, C., Ying, B., Winter, M., Nagel, P., Schuppler, S., and Merz, M. (2021). On the Origin of Reversible and Irreversible Reactions in $LiNi_xCo_{(1-x)/2}Mn_{(1-x)/2}O_2$. Journal of The Electrochemical Society *168*, 120533. 10.1149/1945-7111/ac3c21.

5. Bisogni, V., Catalano, S., Green, R.J., Gibert, M., Scherwitzl, R., Huang, Y., Strocov, V.N., Zubko, P., Balandeh, S., Triscone, J.-M., Sawatzky, G., and Schmitt, T. (2016). Ground-state oxygen holes and the metal–insulator transition in the negative charge-transfer rare-earth nickelates. Nature Communications *7*, 13017. 10.1038/ncomms13017.

6. Abakumov, A.M., Fedotov, S.S., Antipov, E.V., and Tarascon, J.-M. (2020). Solid state chemistry for developing better metal-ion batteries. Nature Communications *11*, 4976. 10.1038/s41467-020-18736-7.

7. Genreith-Schriever, A.R., Banerjee, H., Menon, A.S., Bassey, E.N., Piper, L.F.J., Grey, C.P., and Morris, A.J. (2023). Oxygen hole formation controls stability in $LiNiO_2$ cathodes. Joule *7*, 1623-1640. https://doi.org/10.1016/j.joule.2023.06.017.

8. Shang, T., Xiao, D., Meng, F., Rong, X., Gao, A., Lin, T., Tang, Z., Liu, X., Li, X., Zhang, Q., et al. (2022). Real-space measurement of orbital electron populations for $Li_{1-x}CoO_2$. Nature Communications *13*, 5810. 10.1038/s41467-022-33595-0.

9. Kothalawala, V.N., Suzuki, K., Nokelainen, J., Hyvönen, A., Makkonen, I., Barbiellini, B., Hafiz, H., Tynjälä, P., Laine, P., Välikangas, J., et al. (2024). Compton scattering study of strong orbital delocalization in a Physical Review B *109*, 035139. 10.1103/PhysRevB.109.035139.

10. Fantin, R., Jousseaume, T., Ramos, R., Lefevre, G., Van Roekeghem, A., Rueff, J.-P., and Benayad, A. (2024). Depth-Resolving the Charge Compensation Mechanism from $LiNiO_2$ to NiO_2. ACS Energy Letters, 1507-1515. 10.1021/acsenergylett.4c00360.

11. Abbate, M., de Groot, F.M.F., Fuggle, J.C., Fujimori, A., Tokura, Y., Fujishima, Y., Strebel, O., Domke, M., Kaindl, G., van Elp, J., et al. (1991). Soft-x-ray-absorption studies of the location of extra charges induced by substitution in controlled-valence materials. Physical Review B *44*, 5419-5422. 10.1103/PhysRevB.44.5419.

12. van Elp, J., Wieland, J.L., Eskes, H., Kuiper, P., Sawatzky, G.A., de Groot, F.M.F., and Turner, T.S. (1991). Electronic structure of CoO, Li-doped CoO, and Physical Review B *44*, 6090-6103. 10.1103/PhysRevB.44.6090.

13. van Elp, J., Searle, B.G., Sawatzky, G.A., and Sacchi, M. (1991). Ligand hole induced symmetry mixing of d^8 states in $Li_xNi_{1-x}O$, as observed in Ni 2p x-ray absorption spectroscopy. Solid State Communications *80*, 67-71. https://doi.org/10.1016/0038-1098(91)90600-Z.

14. van Elp, J., Eskes, H., Kuiper, P., and Sawatzky, G.A. (1992). Electronic structure of Li-doped NiO. Physical Review B *45*, 1612-1622. 10.1103/PhysRevB.45.1612.

15. van Veenendaal, M.A., and Sawatzky, G.A. (1994). Doping dependence of Ni 2p x-ray-absorption spectra of MxNi1-xO (M = Li, Na). Physical Review B *50*, 11326-11331. 10.1103/PhysRevB.50.11326.

16. Walroth, R.C., Lukens, J.T., MacMillan, S.N., Finkelstein, K.D., and Lancaster, K.M. (2016). Spectroscopic Evidence for a $3d^{10}$ Ground State Electronic Configuration and Ligand Field Inversion in $[Cu(CF_3)_4]^{1-}$. Journal of the American Chemical Society *138*, 1922-1931. 10.1021/jacs.5b10819.

17. Hoffmann, R., Alvarez, S., Mealli, C., Falceto, A., Cahill, T.J., III, Zeng, T., and Manca, G. (2016). From Widely Accepted Concepts in Coordination Chemistry to Inverted Ligand Fields. Chemical Reviews *116*, 8173-8192. 10.1021/acs.chemrev.6b00251.

18. Snyder, J.P. (1995). Elusiveness of CuIII Complexation; Preference for Trifluoromethyl Oxidation in the Formation of $[Cu^I(CF3)_4]^-$ Salts. Angewandte Chemie International Edition in English *34*, 80-81. https://doi.org/10.1002/anie.199500801.

19. Aullón, G., and Alvarez, S. (2009). Oxidation states, atomic charges and orbital populations in transition metal complexes. Theoretical Chemistry Accounts *123*, 67-73. 10.1007/s00214-009-0537-9.

20. DiMucci, I.M., Titus, C.J., Nordlund, D., Bour, J.R., Chong, E., Grigas, D.P., Hu, C.-H., Kosobokov, M.D., Martin, C.D., Mirica, L.M., et al. (2023). Scrutinizing formally Ni^{IV} centers through the lenses of core spectroscopy, molecular orbital theory, and valence bond theory. Chemical Science *14*, 6915-6929. 10.1039/D3SC02001K.

21. Rana, J., Shi, Y., Zuba, M.J., Wiaderek, K.M., Feng, J., Zhou, H., Ding, J., Wu, T., Cibin, G., Balasubramanian, M., et al. (2018). Role of disorder in limiting the true multi-electron redox in ε-LiVOPO$_4$. Journal of Materials Chemistry A *6*, 20669-20677. 10.1039/C8TA06469E.

22. Gent, W.E., Abate, I.I., Yang, W., Nazar, L.F., and Chueh, W.C. (2020). Design Rules for High-Valent Redox in Intercalation Electrodes. Joule *4*, 1369-1397. 10.1016/j.joule.2020.05.004.

23. Seo, D.H., Lee, J., Urban, A., Malik, R., Kang, S., and Ceder, G. (2016). The structural and chemical origin of the oxygen redox activity in layered and cation-disordered Li-excess cathode materials. Nat Chem *8*, 692-697. 10.1038/nchem.2524.

24. Lu, Z., MacNeil, D.D., and Dahn, J.R. (2001). Layered Cathode Materials Li[Ni$_x$Li$_{(1/3-2x/3)}$Mn$_{(2/3-x/3)}$]O$_2$ for Lithium-Ion Batteries. Electrochemical and Solid-State Letters *4*. 10.1149/1.1407994.

25. Lu, Z., and Dahn, J.R. (2002). Understanding the Anomalous Capacity of Li/Li[Ni$_x$Li$_{(1/3-2x/3)}$Mn$_{(2/3-x/3)}$]O$_2$ Cells Using In Situ X-Ray Diffraction and Electrochemical Studies. Journal of The Electrochemical Society *149*. 10.1149/1.1480014.

26. Luo, K., Roberts, M.R., Hao, R., Guerrini, N., Pickup, D.M., Liu, Y.S., Edstrom, K., Guo, J., Chadwick, A.V., Duda, L.C., and Bruce, P.G. (2016). Charge-compensation in 3d-transition-metal-oxide intercalation cathodes through the generation of localized electron holes on oxygen. Nat Chem *8*, 684-691. 10.1038/nchem.2471.

27. Luo, K., Roberts, M.R., Guerrini, N., Tapia-Ruiz, N., Hao, R., Massel, F., Pickup, D.M., Ramos, S., Liu, Y.S., Guo, J., et al. (2016). Anion Redox Chemistry in the Cobalt Free 3d Transition Metal Oxide Intercalation Electrode Li[Li$_{0.2}$Ni$_{0.2}$Mn$_{0.6}$]O$_2$. J Am Chem Soc *138*, 11211-11218. 10.1021/jacs.6b05111.

28. House, R.A., Rees, G.J., Pérez-Osorio, M.A., Marie, J.-J., Boivin, E., Robertson, A.W., Nag, A., Garcia-Fernandez, M., Zhou, K.-J., and Bruce, P.G. (2020). First-cycle voltage hysteresis in Li-rich 3d cathodes associated with molecular O$_2$ trapped in the bulk. Nature Energy *5*, 777-785. 10.1038/s41560-020-00697-2.

29. Menon, A.S., Johnston, B.J., Booth, S.G., Zhang, L., Kress, K., Murdock, B.E., Paez Fajardo, G., Anthonisamy, N.N., Tapia-Ruiz, N., Agrestini, S., et al. (2023). Oxygen-Redox Activity in Non-Lithium-Excess Tungsten-Doped LiNiO$_2$ Cathode. PRX Energy *2*, 013005. 10.1103/PRXEnergy.2.013005.

30. Mikheenkova, A., Mukherjee, S., Hirsbrunner, M., Törnblom, P., Tai, C.-W., Segre, C.U., Ding, Y., Zhang, W., Asmara, T.C., Wei, Y., et al. (2024). The role of oxygen in automotive grade lithium-ion battery cathodes: an atomistic survey of ageing. Journal of Materials Chemistry A *12*, 2465-2478. 10.1039/D3TA05516G.

31. Juelsholt, M., Chen, J., Pérez-Osorio, M.A., Rees, G.J., De Sousa Coutinho, S., Maynard-Casely, H.E., Liu, J., Everett, M., Agrestini, S., Garcia-Fernandez, M., et al. (2024). Does trapped O$_2$ form in the bulk of LiNiO$_2$ during charging? Energy & Environmental Science. 10.1039/D3EE04354A.

32. Delmas, C., Fouassier, C., and Hagenmuller, P. (1980). Structural classification and properties of the layered oxides. Physica B+C *99*, 81-85. https://doi.org/10.1016/0378-4363(80)90214-4.

33. Menon, A.S., Shah, N., Gott, J.A., Fiamegkou, E., Ogley, M.J.W., Páez Fajardo, G.J., Vaenas, N., Ellis, I., Ravichandran, N., Cloetens, P., et al. (2024). Quantifying Electrochemical Degradation in Single-Crystalline LiNi$_{0.8}$Mn$_{0.1}$Co$_{0.1}$O$_2$–Graphite Pouch Cells through Operando X-Ray and Postmortem Investigations. PRX Energy *3*, 013004. 10.1103/PRXEnergy.3.013004.

34. Dose, W.M., Morzy, J.K., Mahadevegowda, A., Ducati, C., Grey, C.P., and De Volder, M.F.L. (2021). The influence of electrochemical cycling protocols on capacity loss in nickel-rich lithium-ion batteries. Journal of Materials Chemistry A *9*, 23582-23596. 10.1039/D1TA06324C.

35. Zhou, H., Xin, F., Pei, B., and Whittingham, M.S. (2019). What Limits the Capacity of Layered Oxide Cathodes in Lithium Batteries? ACS Energy Letters *4*, 1902-1906. 10.1021/acsenergylett.9b01236.

36. Ruff, Z., Coates, C.S., Märker, K., Mahadevegowda, A., Xu, C., Penrod, M.E., Ducati, C., and Grey, C.P. (2023). O3 to O1 Phase Transitions in Highly Delithiated NMC811 at Elevated Temperatures. Chemistry of Materials *35*, 4979-4987. 10.1021/acs.chemmater.3c00307.

37. Dose, W.M., Li, W., Temprano, I., O'Keefe, C.A., Mehdi, B.L., De Volder, M.F.L., and Grey, C.P. (2022). Onset Potential for Electrolyte Oxidation and Ni-Rich Cathode Degradation in Lithium-Ion Batteries. ACS Energy Letters *7*, 3524-3530. 10.1021/acsenergylett.2c01722.

38. Dose, W.M., Temprano, I., Allen, J.P., Björklund, E., O'Keefe, C.A., Li, W., Mehdi, B.L., Weatherup, R.S., De Volder, M.F.L., and Grey, C.P. (2022). Electrolyte Reactivity at the Charged Ni-Rich Cathode Interface and Degradation in Li-Ion Batteries. ACS Applied Materials & Interfaces *14*, 13206-13222. 10.1021/acsami.1c22812.

39. Zuba, M.J., Grenier, A., Lebens-Higgins, Z., Fajardo, G.J.P., Li, Y., Ha, Y., Zhou, H., Whittingham, M.S., Yang, W., Meng, Y.S., Chapman, K.W., and Piper, L.F.J. (2021). Whither Mn Oxidation in Mn-Rich Alkali-Excess Cathodes? ACS Energy Letters *6*, 1055-1064. 10.1021/acsenergylett.0c02418.

40. Gottschall, R., Schöllhorn, R., Muhler, M., Jansen, N., Walcher, D., and Gütlich, P. (1998). Electronic State of Nickel in Barium Nickel Oxide, $BaNiO_3$. Inorganic Chemistry *37*, 1513-1518. 10.1021/ic9709279.

41. Qiao, R., Wray, L.A., Kim, J.-H., Pieczonka, N.P.W., Harris, S.J., and Yang, W. (2015). Direct Experimental Probe of the Ni(II)/Ni(III)/Ni(IV) Redox Evolution in $LiNi_{0.5}Mn_{1.5}O_4$ Electrodes. The Journal of Physical Chemistry C *119*, 27228-27233. 10.1021/acs.jpcc.5b07479.

42. Wolfman, M., Yu, Y.-S., May, B.M., Lebens-Higgins, Z.W., Sallis, S., Faenza, N.V., Pereira, N., Shirato, N., Rose, V., Shapiro, D.A., et al. (2020). Mapping Competitive Reduction upon Charging in $LiNi_{0.8}Co_{0.15}Al_{0.05}O_2$ Primary Particles. Chemistry of Materials *32*, 6161-6175. 10.1021/acs.chemmater.0c01986.

43. Zhu, J., and Chen, G. (2019). Single-crystal based studies for correlating the properties and high-voltage performance of $Li[Ni_xMn_yCo_{1-x-y}]O_2$ cathodes. Journal of Materials Chemistry A *7*, 5463-5474. 10.1039/C8TA10329A.

44. Homlamai, K., Anansuksawat, N., Joraleechanchai, N., Chiochan, P., Sangsanit, T., Tejangkura, W., Maihom, T., Limtrakul, J., and Sawangphruk, M. (2022). Microcracking of Ni-rich layered oxide does not occur at single crystal primary particles even abused at 4.7 V. Chemical Communications *58*, 11382-11385. 10.1039/D2CC03977J.

45. Ryu, H.-H., Namkoong, B., Kim, J.-H., Belharouak, I., Yoon, C.S., and Sun, Y.-K. (2021). Capacity Fading Mechanisms in Ni-Rich Single-Crystal NCM Cathodes. ACS Energy Letters *6*, 2726-2734. 10.1021/acsenergylett.1c01089.

46. Jung, R., Metzger, M., Maglia, F., Stinner, C., and Gasteiger, H.A. (2017). Oxygen Release and Its Effect on the Cycling Stability of $LiNi_xMn_yCo_zO_2$ (NMC) Cathode Materials for Li-Ion Batteries. Journal of The Electrochemical Society *164*, A1361. 10.1149/2.0021707jes.

47. Oswald, S., and Gasteiger, H.A. (2023). The Structural Stability Limit of Layered Lithium Transition Metal Oxides Due to Oxygen Release at High State of Charge and Its Dependence on the Nickel Content. Journal of The Electrochemical Society *170*, 030506. 10.1149/1945-7111/acbf80.

48. Huang, H., Chang, Y.-C., Huang, Y.-C., Li, L., Komarek, A.C., Tjeng, L.H., Orikasa, Y., Pao, C.-W., Chan, T.-S., Chen, J.-M., et al. (2023). Unusual double ligand holes as catalytic active sites in $LiNiO_2$. Nature Communications *14*, 2112. 10.1038/s41467-023-37775-4.

49. Yoon, W.-S., Kim, K.-B., Kim, M.-G., Lee, M.-K., Shin, H.-J., Lee, J.-M., Lee, J.-S., and Yo, C.-H. (2002). Oxygen Contribution on Li-Ion Intercalation−Deintercalation in $LiCoO_2$ Investigated by O K-Edge and Co L-Edge X-ray Absorption Spectroscopy. The Journal of Physical Chemistry B *106*, 2526-2532. 10.1021/jp013735e.

50. Wu, Z., Zeng, G., Yin, J., Chiang, C.-L., Zhang, Q., Zhang, B., Chen, J., Yan, Y., Tang, Y., Zhang, H., et al. (2023). Unveiling the Evolution of $LiCoO_2$ beyond 4.6 V. ACS Energy Letters, 4806-4817. 10.1021/acsenergylett.3c01954.

51. Hennies, F., Pietzsch, A., Berglund, M., Föhlisch, A., Schmitt, T., Strocov, V., Karlsson, H.O., Andersson, J., and Rubensson, J.-E. (2010). Resonant Inelastic Scattering Spectra of Free Molecules with Vibrational Resolution. Physical Review Letters *104*, 193002. 10.1103/PhysRevLett.104.193002.

52. Hu, E., Li, Q., Wang, X., Meng, F., Liu, J., Zhang, J.-N., Page, K., Xu, W., Gu, L., Xiao, R., et al. (2021). Oxygen-redox reactions in $LiCoO_2$ cathode without O–O bonding during charge-discharge. Joule *5*, 720-736. https://doi.org/10.1016/j.joule.2021.01.006.

53. Shang, H.L. (2014). A survey of functional principal component analysis. AStA Advances in Statistical Analysis *98*, 121-142. 10.1007/s10182-013-0213-1.

54. Lebens-Higgins, Z.W., Chung, H., Zuba, M.J., Rana, J., Li, Y., Faenza, N.V., Pereira, N., McCloskey, B.D., Rodolakis, F., Yang, W., et al. (2020). How Bulk Sensitive is Hard X-ray Photoelectron Spectroscopy: Accounting for the Cathode–Electrolyte Interface when

Addressing Oxygen Redox. The Journal of Physical Chemistry Letters *11*, 2106-2112. 10.1021/acs.jpclett.0c00229.

55. Grenier, A., Kamm, G.E., Li, Y., Chung, H., Meng, Y.S., and Chapman, K.W. (2021). Nanostructure Transformation as a Signature of Oxygen Redox in Li-Rich 3d and 4d Cathodes. Journal of the American Chemical Society *143*, 5763-5770. 10.1021/jacs.1c00497.

56. Rietveld, H.M. (1967). Line profiles of neutron powder-diffraction peaks for structure refinement. Acta Crystallographica *22*, 151-152. https://doi.org/10.1107/S0365110X67000234.

57. Rietveld, H.M. (1969). A profile refinement method for nuclear and magnetic structures. Journal of Applied Crystallography *2*, 65-71. https://doi.org/10.1107/S0021889869006558.

58. Coelho, A.A. (2018). TOPAS and TOPAS-Academic: an optimization program integrating computer algebra and crystallographic objects written in C++. Journal of Applied Crystallography *51*, 210-218. 10.1107/s1600576718000183.

59. Pawley, G.S. (1981). Unit-cell refinement from powder diffraction scans. Journal of Applied Crystallography *14*, 357-361. https://doi.org/10.1107/S0021889881009618.

60. Lebens-Higgins, Z., Chung, H., Temprano, I., Zuba, M., Wu, J., Rana, J., Mejia, C., Jones, M.A., Wang, L., Grey, C.P., et al. (2021). Electrochemical Utilization of Iron IV in the $Li_{1.3}Fe_{0.4}Nb_{0.3}O_2$ Disordered Rocksalt Cathode. Batteries & Supercaps *4*, 771-777. https://doi.org/10.1002/batt.202000318.

61. Dent, A.J., Cibin, G., Ramos, S., Smith, A.D., Scott, S.M., Varandas, L., Pearson, M.R., Krumpa, N.A., Jones, C.P., and Robbins, P.E. (2009). B18: A core XAS spectroscopy beamline for Diamond. Journal of Physics: Conference Series *190*, 012039. 10.1088/1742-6596/190/1/012039.

62. Ravel, B., and Newville, M. (2005). ATHENA, ARTEMIS, HEPHAESTUS: data analysis for X-ray absorption spectroscopy using IFEFFIT. Journal of Synchrotron Radiation *12*, 537-541. https://doi.org/10.1107/S0909049505012719.

63. Newville, M. (2013). Larch: An Analysis Package for XAFS and Related Spectroscopies. Journal of Physics: Conference Series *430*, 012007. 10.1088/1742-6596/430/1/012007.

64. Zabinsky, S.I., Rehr, J.J., Ankudinov, A., Albers, R.C., and Eller, M.J. (1995). Multiple-scattering calculations of x-ray-absorption spectra. Physical Review B *52*, 2995-3009. 10.1103/PhysRevB.52.2995.

65. Zhou, K.-J., Walters, A., Garcia-Fernandez, M., Rice, T., Hand, M., Nag, A., Li, J., Agrestini, S., Garland, P., Wang, H., et al. (2022). I21: an advanced high-resolution resonant inelastic X-ray scattering beamline at Diamond Light Source. Journal of Synchrotron Radiation *29*, 563-580. doi:10.1107/S1600577522000601.

66. Mark Basham, J.F., Michael T. Wharmby, Peter C. Y. Chang, Baha El Kassaby, Matthew Gerring, Jun Aishima, Karl Levik, Bill C. A. Pulford, Irakli Sikharulidze, Duncan Sneddon, Matthew Webber, Sarnjeet S. Dhesi, Francesco Maccherozzi, Olof Svensson, Sandor Brockhauser, Gabor Naray and Alun W. Ashtona (2015). Data Analysis WorkbeNch (DAWN). Journal of Synchrotron Radiation *22* (*3*), 853-858.

67. Haverkort, M.W., Zwierzycki, M., and Andersen, O.K. (2012). Multiplet ligand-field theory using Wannier orbitals. Physical Review B *85*, 165113. 10.1103/PhysRevB.85.165113.

68. Haverkort, M.W., Sangiovanni, G., Hansmann, P., Toschi, A., Lu, Y., and Macke, S. (2014). Bands, resonances, edge singularities and excitons in core level spectroscopy investigated within the dynamical mean-field theory. Europhysics Letters *108*, 57004. 10.1209/0295-5075/108/57004.

69. Smith, R.I., Hull, S., Tucker, M.G., Playford, H.Y., McPhail, D.J., Waller, S.P., and Norberg, S.T. (2019). The upgraded Polaris powder diffractometer at the ISIS neutron source. Rev Sci Instrum *90*, 115101. 10.1063/1.5099568.